INTERNATIONAL JOURNAL FOR NUMERICAL METHODS IN FLUIDS
Int. J. Numer. Meth. Fluids (2012)
Published online in Wiley Online Library (wileyonlinelibrary.com/journal/nmf). DOI: 10.1002/fld.3681

Finite volume methods for unidirectional dispersive wave models

D. Dutykh[1], Th. Katsaounis[2,3,*,†] and D. Mitsotakis[4]

[1]*LAMA UMR 5127, Université de Savoie, CNRS, Campus Scientifique, 73376 Le Bourget-du-Lac, France*
[2]*Department of Applied Mathematics, University of Crete, Heraklion, 71409, Greece*
[3]*Institute of Applied Computational Mathematics (IACM), FORTH, Heraklion, 71110, Greece*
[4]*Institute for Mathematics and its Applications, University of Minnesota 114 Lind Hall, 207 Church Street SE Minneapolis MN 55455*

SUMMARY

We extend the framework of the finite volume method to dispersive unidirectional water wave propagation in one space dimension. In particular, we consider a KdV–BBM-type equation. Explicit and implicit–explicit Runge–Kutta-type methods are used for time discretizations. The fully discrete schemes are validated by direct comparisons to analytic solutions. Invariants' conservation properties are also studied. Main applications include important nonlinear phenomena such as dispersive shock wave formation, solitary waves, and their various interactions. Copyright © 2012 John Wiley & Sons, Ltd.

Received 23 November 2010; Revised 1 February 2012; Accepted 30 March 2012

KEY WORDS: finite volume method; nonlinear dispersive waves; unidirectional propagation; solitary waves; water waves

1. INTRODUCTION

Water wave modeling is a complicated process and usually leads to models that are hard to analyze mathematically as well as to solve numerically. Under certain simplifying assumptions, approximate models, for example, the Korteweg-de Vries (KdV) equation [1], the Benjamin Bona and Mahony (BBM) equation [2], and Boussinesq systems [3–5], are obtained. All these models assume the wave to be weakly nonlinear and weakly dispersive, propagating mainly in one space direction. These approximate models consider mainly unidirectional or bidirectional wave propagation on flat or complex bathymetries.

In this paper, we study the application of some finite volume schemes to a scalar nonlinear dispersive PDE modeling unidirectional wave propagation. Specifically, we consider the KdV–BBM equation in its general form:

$$u_t + \alpha\, u_x + \beta\, u u_x - \gamma\, u_{xxt} + \delta\, u_{xxx} = 0, \tag{1}$$

for $x \in \mathbb{R}$, $t > 0$, where α, β, γ, and δ are positive real numbers [2]. The finite volume method is well known for its accuracy, efficiency, robustness, and excellent local conservative properties. Most often, this method is employed to approximate solutions to hyperbolic conservation laws. The system of nonlinear shallow water equations is a classical example of the successful application of modern finite volume schemes to water wave problems.

A wide range of numerical methods have been employed to compute approximate solutions to dispersive wave equations of KdV–BBM type: finite difference schemes [6, 7], finite element methods [8–10], and spectral methods [11–14]. Recently discontinuous Galerkin schemes have also been employed to dispersive wave equations [15–17] (the list is far from being exhaustive). However, the

*Correspondence to: Th. Katsaounis, Department of Applied Mathematics, University of Crete, Heraklion, 71409 Greece and Institute of Applied Computational Mathematics (IACM), FORTH, Heraklion, 71110, Greece.

†E-mail: thodoros@tem.uoc.gr

application of finite volume or hybrid finite volume/finite difference methods remain most infrequent for this type of problems. To our knowledge, only a few recent works are in this direction [18–23].

In order to apply the finite volume method to the KdV–BBM Equation (1), we rewrite it in a conservative form, including a nontrivial evolution operator and an advective and a dispersive flux function. In the finite volume literature, there exist several ways to approximate these fluxes. For the advective part, we test three different numerical fluxes, each one representing a particular family of finite volume method:

- *average flux* (*m* scheme);
- *central flux* (KT scheme), as a representative of central schemes [24, 25]; and
- *characteristic flux* (CF scheme), as a representative of upwind schemes and linearized Riemann solvers [26, 27].

The *average flux* is simply used to discretize dispersive term, whereas high-order approximations are used for the BBM term (γu_{xxt}). The *central flux* and the *characteristic flux* are widely used in the case of conservation laws. On the other hand, the *average flux*, known to be unstable for conservation laws, performs equally well.

The evaluation of the numerical flux functions require approximate values of the solution at the cell interfaces. The order of the approximation determines the space accuracy of the underlying finite volume scheme. We consider first-order schemes, taking simply piecewise constant approximations, as well as high-order schemes. The high-order accuracy is achieved through application of various reconstruction techniques such as Total Variation Diminishing (TVD) [28], Uniformly Non-oscillatory (UNO) [29], and Weighted essentially non-oscillatory (WENO) [30].

The time discretization of (1) is based on Runge–Kutta (RK) methods. The stability of the resulting system of ODEs depends on the interplay between the BBM term ($\gamma\, u_{xxt}$) and the KdV-type dispersive term ($\delta\, u_{xxx}$). An explicit discretization of the ODE system is sufficient when these terms are of the same order. Thus, strong stability preserving RK (SSP-RK) methods, which preserve the TVD property of the finite volume scheme [31, 32], are used for the explicit discretization.

However, when $\gamma \ll \delta$, the resulting semidiscrete system of ODEs is highly stiff; therefore, implicit methods with strong stability characteristics are preferable. To balance the high computational cost of fully implicit methods and stability considerations, we rely on implicit–explicit (IMEX) RK methods [33]. Indeed IMEX RK methods turned out to be well suited for the time discretization of the KdV–BBM Equation (1), exhibiting excellent stability behavior.

The validated numerical method is applied to study the KdV–BBM Equation (1) in a systematic way through a series of numerical experiments. In particular, we focus on the following issues:

- accuracy of the finite volume method for solitary wave propagation and invariants conservation;
- dispersive shock formation (we underline that the finite element as well as spectral methods break down for this experiment, whereas the finite volume method provides robust and accurate results); and
- interactions of solitary waves (overtaking collisions).

This paper is organized as follows. In Section 2, the governing Equation (1) is presented briefly along with its basic properties. In Section 3, the finite volume discretization as well as fully discrete schemes are presented in details. In Section 4, we validate the discretization procedure by comparisons with analytical solution. Several important test cases are also presented.

2. DISPERSIVE WATER WAVE MODEL EQUATION

We present briefly the mathematical model under consideration and some of its basic properties. The KdV–BBM equation takes the following general form:

$$u_t + \alpha\, u_x + \beta\, u u_x - \gamma\, u_{xxt} + \delta\, u_{xxx} = 0, \tag{2}$$

where $x \in \mathbb{R}$, $t > 0$, u denotes the free surface elevation above the still water level $u = 0$, and α, β, γ, and δ are positive real numbers. Equation (2) incorporates nonlinear and dispersive effects

DOI: 10.1002/fld

and has been suggested as a model for surface water waves in a uniform channel with flat bottom (cf. [2, 34]).

When $\delta = 0$, (2) reduces to the BBM equation [2], whereas taking $\gamma = 0$ leads the celebrated KdV equation [1]. The KdV–BBM model (2) has been studied thoroughly in the past, and the Cauchy problem is known to be well posed in appropriate Sobolev spaces, at least locally in time. Also, the well posedness of some initial boundary value problems, including the initial periodic boundary value problem, can be proved (cf., e.g., [2, 34, 35] and the references therein).

One may easily check that (2) admits exact solitary wave solutions of the form

$$u(x,t) = 3\frac{c_s-\alpha}{\beta}\,\mathrm{sech}^2\left(\frac{1}{2}\sqrt{\frac{c_s-\alpha}{\gamma c_s+\delta}}\,(x-c_s t)\right), \tag{3}$$

which travel rightwards with a given speed c_s. We are going to exploit this solution later in order to validate our discretization procedure and measure the order of convergence of proposed numerical schemes. Further, it is well known that (2) possesses two quantities invariant under its evolution dynamics. Assuming either the solution has compact support or $u \to 0$ $x \to \pm\infty$, one can easily check that quantities

$$I_1(t) = \int_{\mathbb{R}} u(x,t)\,\mathrm{d}x\,, \quad I_2(t) = \int_{\mathbb{R}} \left(u^2(x,t) + \gamma u_x^2(x,t)\right)\,\mathrm{d}x, \tag{4}$$

are conserved in time, that is, $I_1(t) = I_1(0)$ and $I_2(t) = I_2(0), \forall t > 0$. The invariant I_1 reflects the physical property of the mass conservation, whereas invariant I_2 can be assimilated to the generalized kinetic energy. Invariants conservation is a fundamental property important not only for theoretical investigations but also for numerics because it allows to validate numerical schemes and to quantify the accuracy of the obtained results.

For more realistic situations, one has to consider bidirectional models with uniform or variable bathymetry (cf., e.g., [4, 5]). For a systematic numerical study of such Boussinesq-type systems using finite volume methods analogous to those presented in this paper, including the run-up algorithm, we refer to [36].

3. FINITE VOLUME DISCRETIZATION

We proceed to the discretization of (2) by a finite volume method. Our motivation stems from the observation that the KdV–BBM equation can be seen as a dispersive perturbation (because the wave is assumed to be weakly nonlinear and weakly dispersive) of the following inviscid Burgers equation:

$$u_t + \left(\alpha\, u + \frac{\beta}{2}\,u^2\right)_x = 0.$$

Consequently, the proposed finite volume schemes are based on the corresponding schemes for scalar conservation laws. A special treatment is introduced for the discretization of dispersive terms.

Let $\mathcal{T} = \{x_i\}$, $i \in \mathbb{Z}$, be a partition of $\mathbb{R}$ into cells $C_i = \left(x_{i-\frac{1}{2}}, x_{i+\frac{1}{2}}\right)$, where $x_i = \left(x_{i+\frac{1}{2}} + x_{i-\frac{1}{2}}\right)/2$ denotes the midpoint of the cell C_i. Let $\Delta x_i = x_{i+\frac{1}{2}} - x_{i-\frac{1}{2}}$ denote the length of the cell C_i and let $\Delta x_{i+\frac{1}{2}} = x_{i+1} - x_i$. Herein, we assume the partition $\mathcal{T}$ to be uniform, that is, $\Delta x_i = \Delta x_{i+\frac{1}{2}} = \Delta x$, $i \in \mathbb{Z}$. For a scalar function $w(x,t)$, let w_i denote its cell average on C_i:

$$w_i(t) = \frac{1}{\Delta x}\int_{C_i} w(x,t)\,\mathrm{d}x.$$

We rewrite (2) in a conservative-like form:

$$\left(I - \gamma\partial_x^2\right) u_t + [F(u)]_x + [G(u_{xx})]_x = 0, \tag{5}$$

DOI: 10.1002/fld

where the advective flux is $F(u) = \alpha\, u + \frac{\beta}{2}\, u^2$ and the dispersive flux is $G(v) = \delta v$. We underline that F is a convex flux function. A simple integration of (5) over a cell C_i yields

$$\begin{aligned}
&\frac{\mathrm{d}}{\mathrm{d}t}\left[u_i(t) - \frac{\gamma}{\Delta x}\left(u_x\left(x_{i+\frac{1}{2}}, t\right) - u_x\left(x_{i-\frac{1}{2}}, t\right)\right)\right] \\
&\quad + \frac{1}{\Delta x}\left[F\left(u\left(x_{i+\frac{1}{2}}, t\right)\right) - F\left(u\left(x_{i-\frac{1}{2}}, t\right)\right)\right] \\
&\quad + \frac{1}{\Delta x}\left[G\left(u_{xx}\left(x_{i+\frac{1}{2}}, t\right)\right) - G\left(u_{xx}\left(x_{i-\frac{1}{2}}, t\right)\right)\right] = 0,
\end{aligned} \tag{6}$$

where the values of the advective and dispersive fluxes on the cell interfaces have to be properly defined.

3.1. Semidiscrete scheme

We proceed to the construction of the semidiscrete finite volume approximation. Let χ_{C_i} be the characteristic function of the cell C_i. We define a piecewise constant function $u_h(x,t) = \sum_{i\in\mathbb{Z}} U_i(t)\chi_{C_i}(x)$, where $U_i(t)$ are solutions of the following system of ODEs:

$$\frac{\mathrm{d}}{\mathrm{d}t}\left[U_i - \frac{\gamma}{\Delta x}\left(\frac{U_{i+1} - 2U_i + U_{i-1}}{\Delta x}\right)\right] + \frac{1}{\Delta x}\left(\mathcal{F}_{i+\frac{1}{2}} - \mathcal{F}_{i-\frac{1}{2}}\right) + \frac{1}{\Delta x}\left(\mathcal{G}_{i+\frac{1}{2}} - \mathcal{G}_{i-\frac{1}{2}}\right) = 0, \tag{7}$$

with initial conditions defined as a projection onto the space of piecewise constant functions on $\mathcal{T}$:

$$U_i(0) = \frac{1}{\Delta x}\int_{C_i} u(x,0)\,\mathrm{d}x, \quad i \in \mathbb{Z}.$$

In (7), $\mathcal{F}$ and $\mathcal{G}$ denote the advective and the (KdV-type) dispersive numerical fluxes, respectively. More specifically, $\mathcal{F}_{i+\frac{1}{2}} = \mathcal{F}\left(U^L_{i+\frac{1}{2}}, U^R_{i+\frac{1}{2}}\right)$ and $\mathcal{G}_{i+\frac{1}{2}} = \mathcal{G}\left(W^L_{i+\frac{1}{2}}, W^R_{i+\frac{1}{2}}\right)$ are approximations of $F\left(u\left(x_{i+\frac{1}{2}}, t\right)\right)$ and $G\left(u_{xx}\left(x_{i+\frac{1}{2}}, t\right)\right)$, respectively, at cell interfaces. Values $U^L_{i+\frac{1}{2}}, U^R_{i+\frac{1}{2}}$ are approximations to the point value $u\left(x_{i+\frac{1}{2}}, t\right)$ from cells C_i and C_{i+1}, respectively, whereas $W^L_{i+\frac{1}{2}}$ and $W^R_{i+\frac{1}{2}}$ are corresponding approximations to the point value of the second derivative $u_{xx}\left(x_{i+\frac{1}{2}}, t\right)$. All quantities $U^L_{i+\frac{1}{2}}$ and $U^R_{i+\frac{1}{2}}$ as well as $W^L_{i+\frac{1}{2}}$ and $W^R_{i+\frac{1}{2}}$ are computed by a reconstruction process described in Section 3.1.2.

3.1.1. Advective and dispersive numerical fluxes. Over the last 20 years, numerous numerical fluxes $\mathcal{F}$ have been proposed to discretize advective operators [37–41]. We select three quite different flux functions. Namely, we consider a simple *average* flux $\mathcal{F}^m$, a *central*-type flux $\mathcal{F}^{\mathrm{KT}}$ [24, 25], and a *characteristic* flux $\mathcal{F}^{\mathrm{CF}}$ [26, 27, 41]:

$$\mathcal{F}^m(U,V) = F\left(\frac{U+V}{2}\right), \tag{8}$$

$$\mathcal{F}^{\mathrm{KT}}(U,V) = \frac{1}{2}\{[F(U) + F(V)] - \mathcal{A}(U,V)[V-U]\}, \tag{9}$$

$$\mathcal{F}^{\mathrm{CF}}(U,V) = \frac{1}{2}\{[F(U) + F(V)] - \mathcal{A}(U,V)[F(V) - F(U)]\}. \tag{10}$$

The *average* flux is perhaps the simplest one and is known to be unconditionally unstable for nonlinear conservation laws. However, this flux shows very good performance for dispersive waves (see Section 4).

The *central* flux is of Lax–Friedrichs type and is a representative of the family of central schemes. The operator $\mathcal{A}$ in the KT scheme is related to characteristic speeds of the flow and is given by this expression:

$$\mathcal{A}(U,V) = \max\left[\left|F'(U)\right|, \left|F'(V)\right|\right]. \tag{11}$$

DOI: 10.1002/fld

The *characteristic* flux function is somehow similar to the Roe scheme [37], and the operator $\mathcal{A}$ in this case is defined as

$$\mathcal{A}(U,V) = \operatorname{sign}\left(F'\left(\frac{U+V}{2}\right)\right) = \operatorname{sign}\left(\alpha + \beta\frac{U+V}{2}\right). \tag{12}$$

For the dispersive numerical flux $\mathcal{G}$, we choose to work with the average flux function (8):

$$\mathcal{G}(W,R) = \delta\,\frac{W+R}{2}, \tag{13}$$

where W and R are standard central approximations of the second derivative from each side. The numerical flux $\mathcal{G}$ can be evaluated using either simple cell averages, denoted by $\mathcal{G}^m$, or higher-order approximation based on a reconstruction procedure, denoted by $\mathcal{G}^{lm}$.

3.1.2. Reconstruction process. The values $U^L_{i+\frac{1}{2}}$ and $U^R_{i+\frac{1}{2}}$ are approximations to $u\left(x_{i+\frac{1}{2}},t\right)$ from cells C_i and C_{i+1}, respectively. The simplest choice is to take the piecewise constant approximation in each cell:

$$U^L_{i+\frac{1}{2}} = U_i, \quad U^R_{i+\frac{1}{2}} = U_{i+1}. \tag{14}$$

The resulting semidiscrete finite volume scheme is formally first-order accurate in space. To achieve a higher-order accuracy in space, we have to adopt more elaborated reconstruction process. The main idea is to use the cell averages U_i to reconstruct more accurate approximation to the solution at cell interfaces $u(x_{i+\frac{1}{2}},t)$. For this purpose, we consider three different reconstruction methods: the classical MUSCL-type (TVD2) piecewise linear reconstruction [42,43], the UNO2 reconstruction [29], and WENO-type reconstructions [30].

- The classical TVD2 scheme uses a linear reconstruction:

$$U^L_{i+\frac{1}{2}} = U_i + \frac{1}{2}\phi(r_i)(U_{i+1}-U_i), \quad U^R_{i+\frac{1}{2}} = U_{i+1} - \frac{1}{2}\phi(r_{i+1})(U_{i+2}-U_{i+1}), \tag{15}$$

  where $r_i = \frac{U_i - U_{i-1}}{U_{i+1}-U_i}$ and ϕ is an appropriate slope limiter function [28]. There exist many possible choices of the slope limiter. Some of the usual choices are

  - MinMod limiter: $\phi(\theta) = \max(0,\min(1,\theta))$;
  - van Leer limiter: $\phi(\theta) = \frac{\theta+|\theta|}{1+|\theta|}$;
  - monotonized central limiter: $\phi(\theta) = \max\left(0,\min((1+\theta)/2,2,2\theta)\right)$; and
  - van Albada limiter: $\phi(\theta) = \frac{\theta+\theta^2}{1+\theta^2}$.

  The last three limiters have been shown to produce sharper resolution of discontinuities and, in our case, less dissipative numerical results. The TVD2 reconstruction is formally second-order accurate except at local extrema where it reduces to the first order. Reconstructions considered here were proposed to remove this shortcoming.
- The UNO2, like the TVD2, is also a linear reconstruction process that is second-order accurate even at local extrema. The values $U^L_{i+\frac{1}{2}}$ and $U^R_{i+\frac{1}{2}}$ are defined as

$$U^L_{i+\frac{1}{2}} = U_i + \frac{1}{2}S_i, \quad U^R_{i+\frac{1}{2}} = U_{i+1} - \frac{1}{2}S_{i+1}, \tag{16}$$

  where

$$S_i = m\left(S_i^+, S_i^-\right), \quad S_i^{\pm} = d_{i\pm\frac{1}{2}}U \mp \frac{1}{2}D_{i\pm\frac{1}{2}}U,$$
$$d_{i+\frac{1}{2}}U = U_{i+1}-U_i, \quad D_{i+\frac{1}{2}}U = m(D_iU, D_{i+1}U),$$
$$D_iU = U_{i+1} - 2U_i + U_{i-1}, \quad m(x,y) = \frac{1}{2}(\operatorname{sign}(x)+\operatorname{sign}(y))\min(|x|,|y|)$$

  The UNO2 reconstruction is formally second-order accurate even at local extrema.

DOI: 10.1002/fld

- We also consider WENO-type reconstructions [30, 44]. Namely, we implement the third-order and fifth-order accurate WENO methods, hereafter referred to as WENO3 and WENO5, respectively. For the sake of clarity, we present here only WENO3 scheme. First of all, we compute the third-order reconstructed values:

$$U^{(0)}_{i+\frac{1}{2}} = \frac{1}{2}(U_i + U_{i+1}), \quad U^{(1)}_{i+\frac{1}{2}} = \frac{1}{2}(-U_{i-1} + 3U_i),$$
$$U^{(0)}_{i-\frac{1}{2}} = \frac{1}{2}(3U_i - U_{i+1}), \quad U^{(1)}_{i-\frac{1}{2}} = \frac{1}{2}(U_{i-1} + U_i).$$

  Then, we define the smoothness indicators

$$\beta_0 = (U_{i+1} - U_i)^2, \quad \beta_1 = (U_i - U_{i-1})^2,$$

  and constants $d_0 = \frac{2}{3}$, $d_1 = \frac{1}{3}$, $\tilde{d}_0 = d_1$, and $\tilde{d}_1 = d_0$. The weights are defined as

$$\omega_0 = \frac{\alpha_0}{\alpha_0 + \alpha_1}, \quad \omega_1 = \frac{\alpha_0}{\alpha_0 + \alpha_1}, \quad \tilde{\omega}_0 = \frac{\tilde{\alpha}_0}{\tilde{\alpha}_0 + \tilde{\alpha}_1}, \quad \tilde{\omega}_1 = \frac{\tilde{\alpha}_1}{\tilde{\alpha}_0 + \tilde{\alpha}_1},$$

  where $\alpha_i = \frac{d_i}{\epsilon + \beta_i}$, $\tilde{\alpha}_i = \frac{\tilde{d}_i}{\epsilon + \beta_i}$, and ϵ is a small, positive number (in our computations, we set $\epsilon = 10^{-15}$).

  Finally, the reconstructed values are given by formulas:

$$U^L_{i+\frac{1}{2}} = \sum_{r=0}^{1} \omega_r U^{(r)}_{i+\frac{1}{2}}, \quad U^R_{i-\frac{1}{2}} = \sum_{r=0}^{1} \tilde{\omega}_r U^{(r)}_{i-\frac{1}{2}}. \tag{17}$$

Remark 1
The elliptic operator approximation in (7) is only second-order accurate. In the case where a high-order WENO reconstruction is used, we need to increase also the elliptic solver accuracy, for example, the following semidiscrete scheme:

$$\frac{d}{dt}\left[\frac{U_{i-1} + 10U_i + U_{i+1}}{12} - \gamma \frac{U_{i+1} - 2U_i + U_{i-1}}{\Delta x^2}\right] + \frac{\mathcal{H}_{i-1} + 10\mathcal{H}_i + \mathcal{H}_{i+1}}{12} = 0 \tag{18}$$

where $\mathcal{H}_i = \frac{1}{\Delta x}\left(\mathcal{F}_{i+\frac{1}{2}} - \mathcal{F}_{i-\frac{1}{2}}\right) + \frac{1}{\Delta x}\left(\mathcal{G}_{i+\frac{1}{2}} - \mathcal{G}_{i-\frac{1}{2}}\right)$ is a fourth-order approximation. Thus, in the WENO3 case, a global third-order accuracy is observed, whereas for WENO5 interpolation, we profit only locally by the fifth-order accuracy of the reconstruction (cf. Section 4.1).

Remark 2
In computation of the dispersive flux, we distinguish between the simple averaging of cell-centered values in $\mathcal{G}^m$ and $\mathcal{G}^{lm}$, where higher-order reconstructions of the second-order derivatives are used.

3.2. Fully discrete schemes

We consider now fully discrete schemes for the ODE system (7). The time discretization is based on RK-type methods. Explicit schemes based on TVD-preserving RK methods are presented. In certain cases where stiffness becomes dominant, we use an IMEX strategy on the basis of IMEX-type RK methods.

3.2.1. Explicit schemes. The initial value problem (7) can be discretized by various methods. When the parameter γ is of the same order as δ, the system of ODEs appeared to be nonstiff and therefore can be integrated numerically by any explicit time stepping method. We use a special class of RK methods that preserve the TVD property of the finite volume scheme [31, 32, 45].

Let Δt be the temporal step size and let $t^{n+1} = t^n + \Delta t$, $n \geqslant 0$, be discrete time levels; then, (7) is an initial value problem of the form

$$\mathbf{T}\mathbf{U}' = L(\mathbf{U}), \tag{19}$$

DOI: 10.1002/fld

where $\mathbf{U} = \{U_i\},\ i \in \mathbb{Z}$, $\mathbf{T} = \mathbf{I} + [-\gamma, 2\gamma, -\gamma]/\Delta x^2$ is a tridiagonal matrix, and L is a nonlinear operator incorporating the contribution of the numerical fluxes $\mathcal{F}$, and $\mathcal{G}$. Assuming at time t^n, $\mathbf{U}^n$ is known, then $\mathbf{U}^{n+1}$ is defined by

$$\begin{aligned} \mathbf{U}^{n+1} &= \mathbf{U}^n - \frac{\Delta t}{\Delta x} \sum_{j=1}^{s} b_j \mathbf{T}^{-1} L\left(\mathbf{U}^{n,j}\right), \\ \mathbf{U}^{n,j} &= \mathbf{U}^n - \frac{\Delta t}{\Delta x} \sum_{\ell=1}^{s-1} a_{j\ell} \mathbf{T}^{-1} L\left(\mathbf{U}^{n,\ell}\right), \end{aligned} \tag{20}$$

where the set of constants $A = (a_{j\ell})$ and $b = (b_1, \ldots, b_s)$ define an s-stage RK method. The following *tableau* are examples of explicit TVD RK methods, which are of second and third orders, respectively.

$$\begin{array}{ccc|c} 0 & 0 & & 0 \\ 1 & 0 & & 1 \\ \hline \frac{1}{2} & \frac{1}{2} & & \end{array} \qquad \begin{array}{ccc|c} 0 & 0 & 0 & 0 \\ 1 & 0 & 0 & 1 \\ \frac{1}{4} & \frac{1}{4} & 0 & \frac{1}{2} \\ \hline \frac{1}{6} & \frac{1}{6} & \frac{2}{3} & \end{array} \tag{21}$$

In our computations, we mainly use the three-stage third-order method.

3.2.2. Implicit–explicit schemes. As the parameter γ decreases to zero, the semidiscretization of the KdV–BBM equation leads to a stiff system of ODEs. To solve efficiently this system, we apply an IMEX-type RK method [33]. The linear dispersive terms are treated in an implicit way, whereas the rest of the terms are treated explicitly. Numerical evidence shows that IMEX methods exhibit excellent stability and handle stiffness in an efficient and robust way even in the limiting case $\gamma = 0$.

We consider an s-stage diagonally implicit RK (DIRK) method, properly chosen, that is given by the *tableau*

$$\begin{array}{c|c} A & \tau \\ \hline b & \end{array} = \begin{array}{cccc|c} a_{11} & 0 & \cdots & 0 & \tau_1 \\ a_{21} & a_{22} & \cdots & 0 & \tau_2 \\ \vdots & \vdots & \ddots & \vdots & \vdots \\ a_{s1} & a_{s2} & \cdots & a_{ss} & \tau_s \\ \hline b_1 & b_2 & \cdots & b_s & \end{array} \tag{22}$$

and an $s+1$ explicit RK (ERK) method

$$\begin{array}{c|c} \hat{A} & \hat{\tau} \\ \hline \hat{b} & \end{array} = \begin{array}{ccccc|c} 0 & 0 & \cdots & 0 & 0 & 0 \\ \hat{a}_{11} & 0 & \cdots & 0 & 0 & \hat{\tau}_1 \\ \hat{a}_{21} & \hat{a}_{22} & \cdots & 0 & 0 & \hat{\tau}_2 \\ \vdots & \vdots & \ddots & \vdots & \vdots & \vdots \\ \hat{a}_{s1} & \hat{a}_{s2} & \cdots & \hat{a}_{ss} & 0 & \hat{\tau}_s \\ \hline \hat{b}_1 & \hat{b}_2 & \cdots & \hat{b}_s & 0 & \end{array}. \tag{23}$$

We rewrite system (19) in the form

$$\mathbf{T}\mathbf{U}' = \mathcal{F}(\mathbf{U}) + \mathbf{D}\mathbf{U}, \tag{24}$$

where $\mathbf{D}$ is the five-diagonal matrix $\delta[-1/2, 1, 0, -1, 1/2]/\Delta x^3$ coming from the discretization of the KdV term when we use the numerical flux function $\mathcal{G}^m$. Then, the fully discrete scheme can be

DOI: 10.1002/fld

written in the form

$$(\mathbf{T}+\Delta t a_{ii}\mathbf{D})\mathbf{U}^{(i)} = \mathbf{T}\mathbf{U}^n - \Delta t\sum_{j=1}^{i}\hat{a}_{ij}\mathcal{F}\left(\mathbf{U}^{(j)}\right) - \Delta t\sum_{j=1}^{i-1}a_{ij}\mathbf{D}\mathbf{U}^{(j)}, \quad i=1,\dots,s, \tag{25}$$

$$\mathbf{T}\mathbf{U}^{n+1} = \mathbf{T}\mathbf{U}^n - \Delta t\sum_{j=1}^{s}\hat{b}_{j}\mathcal{F}\left(\mathbf{U}^{(j)}\right) - \Delta t\sum_{j=1}^{s}b_{j}\mathbf{D}\mathbf{U}^{(j)}. \tag{26}$$

We employ four IMEX RK methods of different numbers of stages, orders of accuracy, and stability properties. In particular, we consider the following pairs [33]:

- A two-stage third-order DIRK method and a corresponding three-stage third-order accurate ERK method with $\gamma = \left(3+\sqrt{3}\right)/6$. The resulting IMEX method is third-order accurate.

$$\begin{array}{cc|c} \gamma & 0 & \gamma \\ 1-2\gamma & \gamma & 1-\gamma \\ \hline \frac{1}{2} & \frac{1}{2} & \end{array}, \qquad \begin{array}{ccc|c} 0 & 0 & 0 & 0 \\ \gamma & 0 & 0 & \gamma \\ 1-\gamma & 2(1-\gamma) & 0 & 1-\gamma \\ \hline 0 & \frac{1}{2} & \frac{1}{2} & \end{array}. \tag{27}$$

- A two-stage second-order DIRK method, which is stiffly accurate, with $\gamma = \left(2-\sqrt{2}\right)/2$. The corresponding ERK is a three-stage second-order accurate method with $\delta = -2\sqrt{2}/3$. The resulting IMEX combination is second-order accurate.

$$\begin{array}{cc|c} \gamma & 0 & \gamma \\ 1-\gamma & \gamma & 1 \\ \hline 1-\gamma & \gamma & \end{array}, \qquad \begin{array}{ccc|c} 0 & 0 & 0 & 0 \\ \gamma & 0 & 0 & \gamma \\ \delta & 1-\delta & 0 & 1 \\ \hline 0 & 1-\gamma & \gamma & \end{array}. \tag{28}$$

- A three-stage third-order DIRK stiffly accurate method with larger dissipative region than (28). The corresponding ERK is a three-stage third-order method. The resulting IMEX pair is third-order accurate.

$$\begin{array}{ccc|c} 0.4358665215 & 0 & 0 & 0.4358665215 \\ 0.2820667392 & 0.4358665215 & 0 & 0.7179332608 \\ 1.208496649 & -0.644363171 & 0.4358665215 & 1 \\ \hline 1.208496649 & -0.644363171 & 0.4358665215 & \end{array},$$

$$\begin{array}{cccc|c} 0 & 0 & 0 & 0 & 0 \\ 0.4358665215 & 0 & 0 & 0 & 0.4358665215 \\ 0.3212788860 & 0.3966543747 & 0 & 0 & 0.7179332608 \\ -0.105858296 & 0.5529291479 & 0.5529291479 & 0 & 1 \\ \hline 0 & 1.208496649 & -0.644363171 & 0.4358665215 & \end{array}. \tag{29}$$

- A four-stage, L-stable DIRK method with rational coefficients. The corresponding ERK is a five-stage third-order method. The resulting IMEX method is of third order.

$$\begin{array}{cccc|c} \frac{1}{2} & 0 & 0 & 0 & \frac{1}{2} \\ \frac{1}{6} & \frac{1}{2} & 0 & 0 & \frac{2}{3} \\ -\frac{1}{2} & \frac{1}{2} & \frac{1}{2} & 0 & \frac{1}{2} \\ \frac{3}{2} & -\frac{3}{2} & \frac{1}{2} & \frac{1}{2} & 1 \\ \hline \frac{3}{2} & -\frac{3}{2} & \frac{1}{2} & \frac{1}{2} & \end{array}, \qquad \begin{array}{ccccc|c} 0 & 0 & 0 & 0 & 0 & 0 \\ \frac{1}{2} & 0 & 0 & 0 & 0 & \frac{1}{2} \\ \frac{11}{18} & \frac{1}{18} & 0 & 0 & 0 & \frac{2}{3} \\ \frac{5}{6} & -\frac{5}{6} & \frac{1}{2} & 0 & 0 & \frac{1}{2} \\ \frac{1}{4} & \frac{7}{4} & \frac{3}{4} & -\frac{7}{4} & 0 & 1 \\ \hline \frac{1}{4} & \frac{7}{4} & \frac{3}{4} & -\frac{7}{4} & 0 & \end{array}. \tag{30}$$

We tested these IMEX methods in the case of the KdV equation with $\alpha=\beta=\delta=1$ and $\gamma=0$. In Table I, we summarize the constraints for the time step Δt, purely in terms of Δx, to obtain a stable solution. IMEX methods (29) and (30) exhibit excellent stability behavior.

DOI: 10.1002/fld

Table I. Stability of IMEX for the KdV equation ($\alpha = \beta = \delta = 1$ and $\gamma = 0$).

Method	$\Delta t/\Delta x \leqslant$
(27)	1/4
(28)	1/5
(29)	1
(30)	1

4. NUMERICAL RESULTS

In this section, we present a series of numerical results aiming to show the performance and robustness of discretization procedures described previously. There are many possible combinations of numerical fluxes, types of reconstruction, and slope limiter functions. We begin by examining the accuracy of the methods by measuring the convergence rates in Section 4.1 and the preservation of the invariants in Section 4.2. The ability of the schemes to capture a solitary wave solution is demonstrated in Section 4.3. Solitary wave collisions are studied in Section 4.4. Finally, a dispersive shock wave formation is investigated in Section 4.5.

Remark 3
The solution of the linear system involved in (19) and (25) is obtained by a variation of Gauss elimination for tridiagonal systems with computational complexity $\mathcal{O}(d)$, with d being the dimension of the system.

4.1. Rates of convergence and accuracy test

We consider an initial value problem for (2) with periodic boundary conditions in $[-100, 100]$. We take for simplicity $\alpha = \beta = \gamma = \delta = 1$ and consider a solitary wave solution of the form (3) with $c_s = 1.1$. We take a uniform mesh $h = \Delta x = 200/N$ and compute the solution up to $T = 100$ by using the three-stage third-order explicit SSP-RK method (21) with time step $\Delta t = T/M$. The errors are measured using the discrete scaled norms E_h^2 and E_h^∞ [16]:

$$E_h^2(k) = \|U^k\|_h / \|U^0\|_h, \quad \|U^k\|_h = \left(\sum_{i=1}^{N} \Delta x |U_i^k|^2 \right)^{1/2},$$
$$E_h^\infty(k) = \|U^k\|_{h,\infty} / \|U^0\|_{h,\infty}, \quad \|U^k\|_{h,\infty} = \max_{i=1,\ldots,N} |U_i^k|,$$

where $U^k = \{U_i^k\}_{i=1}^N$ denotes the solution of the fully discrete scheme (20) at the time $t^k = k\,\Delta t$. The numerical rate of convergence is defined by

$$\text{Rate} = \frac{\log(E_{h_1}/E_{h_2})}{\log(h_1/h_2)},$$

for two different mesh sizes h_1 and h_2.

We perform several tests by using the TVD2, UNO2, and WENO3 reconstructions. Numerical solutions are computed with CF, KT, or average fluxes. Table II shows the rates of convergence for the CF scheme along with UNO2 and WENO3 reconstructions. We observe the theoretical second-order convergence for the average, TVD2 (not reported), and UNO2 schemes. The WENO3 reconstruction in conjunction with the improved elliptic inversion scheme (18) gives us the expected third-order convergence. Rates in Table II are obtained with the most dissipative MinMod limiter function, whereas slightly sharper results are yielded by other limiters. Moreover, the convergence results for the average m flux and the KT numerical flux are qualitatively identical to those of CF. Analogous convergence rates were obtained using the IMEX methods.

DOI: 10.1002/fld

Table II. Rates of convergence: CF flux.

	Δx	Rate $\left(E_h^2\right)$	Rate $\left(E_h^\infty\right)$
UNO2 MinMod	0.5	2.000	2.015
	0.25	2.001	2.014
	0.125	2.001	2.012
	0.0625	2.001	2.010
	0.03125	2.001	2.008
WENO3	0.5	2.604	2.561
	0.25	2.790	2.810
	0.125	2.905	2.913
	0.0625	2.974	2.981
	0.03125	2.968	2.995

4.2. Invariants preservation

As already mentioned in Section 2, (2) admits at least two quantities (4), which remain constant under the equation dynamics. We investigate the conservation of these quantities by computing their discrete counterparts:

$$I_1^h = \Delta x \sum_i U_i, \quad I_2^h = \Delta x \sum_i \left(U_i^2 + \gamma \left[\frac{U_{i+1} - U_i}{\Delta x} \right]^2 \right). \tag{31}$$

The observation of invariants during numerical computations (20) may also give an idea on the overall discretization accuracy.

The initial value problem for (2) with periodic boundary conditions is considered. We set $\alpha = \beta = \gamma = \delta = 1$ and consider a solitary wave solution with celerity $c_s = 1.5$. We compute its evolution up to $T = 200$ by using $\Delta x = 0.1$ and $\Delta t = \Delta x/2$.

The first observation is that the mass of the solitary wave $I_1^h = 13.41640786499$ is preserved in all computations independently from the choice of any of the numerical flux, reconstruction method, or the slope limiter function.

The behavior of I_2^h is quite different. Figure 1 shows the evolution of the solitary wave amplitude and of the invariant I_2^h. The numerical solution is obtained using $\mathcal{F}^m$, $\mathcal{F}^{\mathrm{CF}}$, and $\mathcal{F}^{\mathrm{KT}}$ numerical fluxes along with TVD2 and UNO2 reconstructions. The limiter MinMod is used, and the dispersive flux is computed with $\mathcal{G}^{lm}$ flux function. The behavior of CF and KT schemes is almost identical. Perhaps, the CF scheme is slightly less dissipative than the KT scheme. However, the m scheme appears to be the least dissipative.

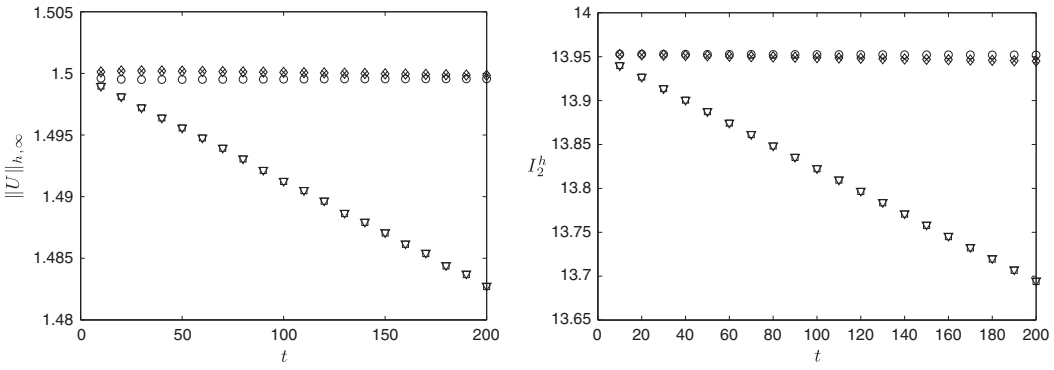

(a) Solitary wave amplitude (b) Invariant I_2^h

Figure 1. Evolution of (a) solitary wave amplitude and (b) invariant I_2^h with G^{lm} flux and MinMod limiter. $\triangledown$: CF-TVD2; $\diamond$: CF-UNO2; $\square$: KT-TVD2; $\times$: KT-UNO2; $\circ$: m scheme.

DOI: 10.1002/fld

For both KT and CF fluxes, the TVD2 reconstruction preserves neither the invariant I_2^h nor the amplitude of the solitary wave. At the same time, UNO2 reconstruction shows excellent behavior. Despite its simplicity, the m scheme, using $\mathcal{F}^m$ and $\mathcal{G}^m$, performs very well too in preserving I_2^h and the solitary wave amplitude.

In Figure 2, we show the influence of the choice of dispersive fluxes $\mathcal{G}^m$ and $\mathcal{G}^{lm}$. One observes that G^{lm} flux shows better behavior than the simpler G^m flux. A comparable performance is achieved with CF scheme using WENO3 and WENO5 reconstructions.

Finally, in Figure 3, we show a comparison between the various slope limiter functions (MinMod, van Albada, van Leer, and monotonized central) tested with CF scheme. MinMod limiter exhibits a small dissipative effect, whereas other limiters we tested show comparable behavior. The choice of the time stepping method does not induce any difference.

4.3. Propagation of solitary waves

We continue the presentation of numerical results by the classical test case of a solitary wave propagation. This class of solutions (3) plays a very important role in the nonlinear physics, and any practical numerical scheme should be able to compute with good accuracy this type of solutions. For simplicity, we will set to unity all coefficients $\alpha = \beta = \gamma = \delta = 1$ in (2).

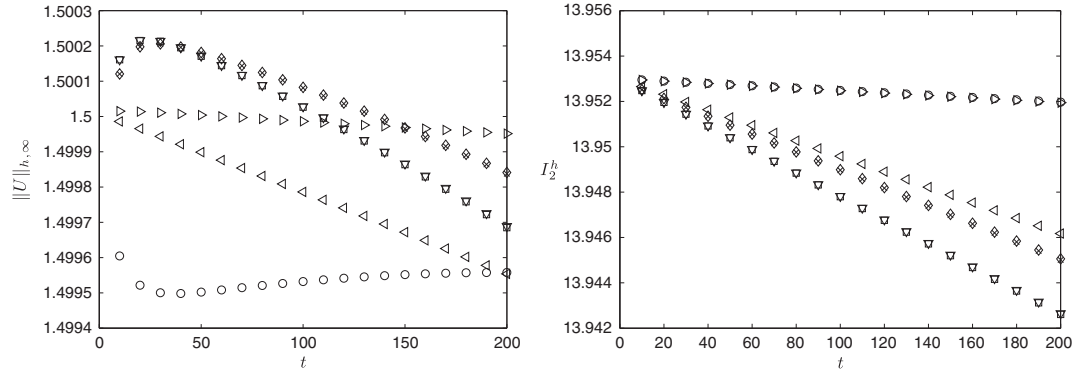

(a) Solitary wave amplitude (b) Invariant I_2^h

Figure 2. Evolution of (a) solitary wave amplitude and (b) invariant I_2^h, UNO2 reconstruction with MinMod limiter. $\triangledown$: $\mathcal{F}^{\mathrm{CF}} - \mathcal{G}^{lm}$; $\diamond$: $\mathcal{F}^{\mathrm{CF}} - \mathcal{G}^{m}$; $\square$: $\mathcal{F}^{\mathrm{KT}} - \mathcal{G}^{lm}$; $\times$: $\mathcal{F}^{\mathrm{KT}} - \mathcal{G}^{m}$; $\triangleleft$: $\mathcal{F}^{\mathrm{CF}}$ – WENO3; $\triangleright$: $\mathcal{F}^{\mathrm{CF}}$ – WENO5; $\circ$: $\mathcal{F}^{m} - \mathcal{G}^{m}$. (Notice the scale difference on the vertical axis with respect to Figure 1.)

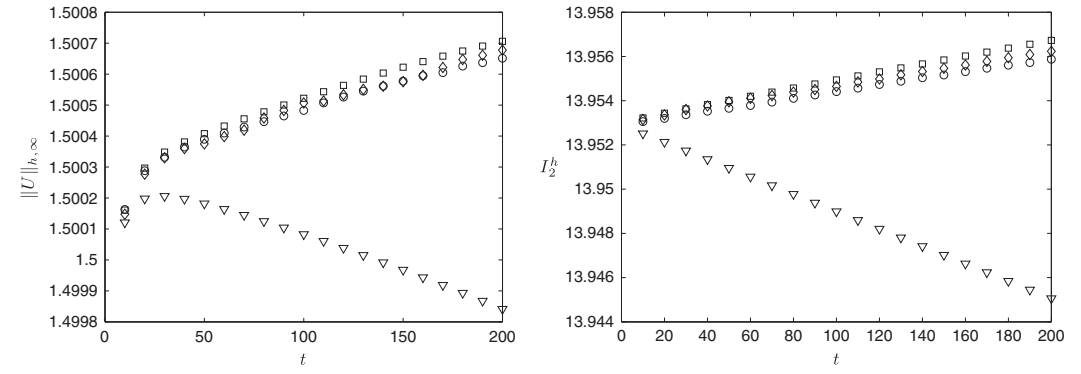

(a) Solitary wave amplitude (b) Invariant I_2^h

Figure 3. Evolution of (a) solitary wave amplitude and (b) invariant I_2^h, $\mathcal{F}^{\mathrm{CF}}$–$\mathcal{G}^{lm}$ fluxes and UNO2 reconstruction: $\triangledown$: MinMod; $\diamond$: monotonized central; $\square$: van Albada; $\circ$: van Leer. (Notice the scale difference on the vertical axis with respect to Figure 1.)

DOI: 10.1002/fld

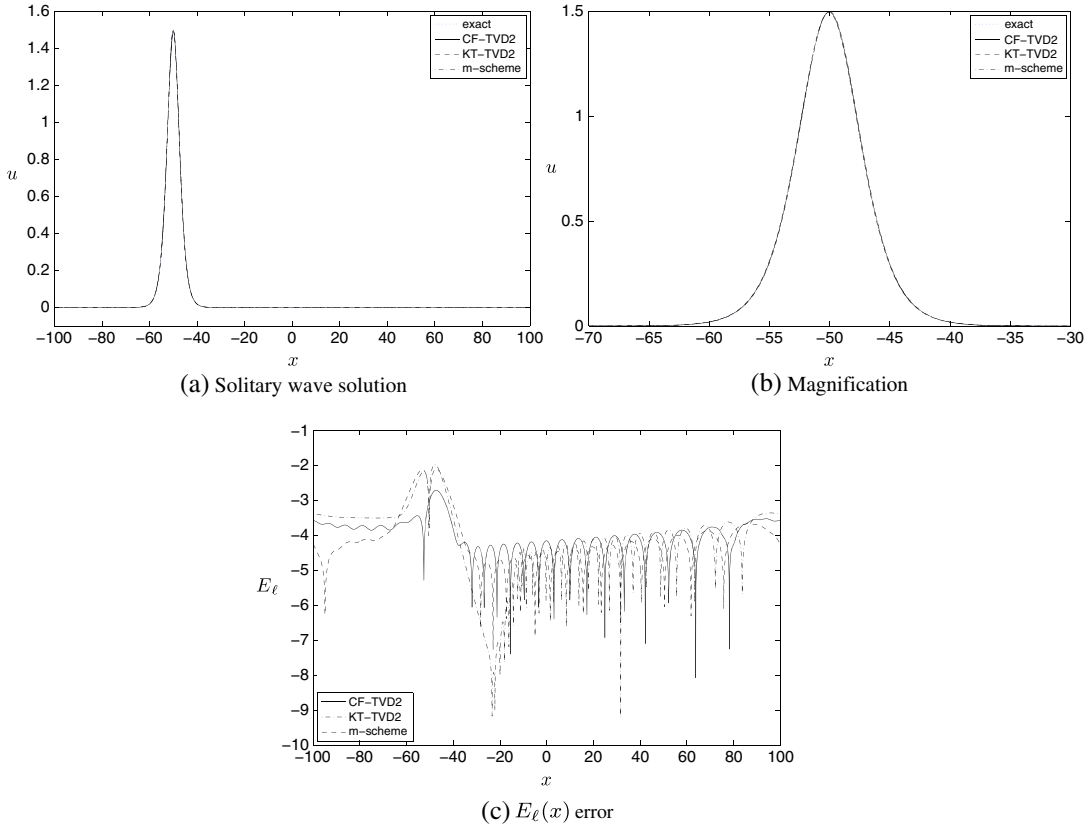

(a) Solitary wave solution

(b) Magnification

(c) $E_\ell(x)$ error

Figure 4. Comparison between the analytical and numerical solutions: (a) solitary wave solution, (b) magnification, and (c) $E_\ell(x)$ error. . . . : analytical solution; —: CF-TVD2; - -: KT-TVD2; -·-: m scheme.

A large-amplitude solitary wave travels rightwards with the speed $c_s = 1.5$. Its propagation is computed up to $T = 100$ with discretization parameters $\Delta x = \Delta t = 0.1$ using KT and CF numerical fluxes and TVD2 reconstruction. In both cases, we use the van Albada limiter. In Figure 4, we compare the analytical solution with the numerical one. Figure 4(b) is a magnification of the solitary pulse, showing that the solitary wave shape is perfectly retained. Also, we note that up to the graphical resolution, all curves are undistinguishable. In order to observe the differences between these solutions, we present in Figure 4(c) the error $E_\ell = \log_{10} |u_{\text{exact}}(x, 100) - U(x, 100)|$. This shows that the difference between the numerical solution and the exact solution is analogous in all the cases and is very small.

The behavior of the numerical solutions can be better understood by analyzing the so-called effective equation, that is, the PDE that the numerical scheme satisfies up to the order of the method. Obtaining an effective equation is not always feasible. In the case of the m scheme for the KdV–BBM Equation (2), the numerical solution u_h satisfies the following *effective* equation:

$$u_{h,t} + \alpha u_{h,x} + \beta u_h u_{h,x} - \gamma u_{h,xxt} + \delta u_{h,xxx} + \Delta x^2 \left(\frac{\alpha}{6} u_{h,xxx} + \frac{\beta}{6} u_h u_{h,xxx} + \frac{\beta}{4} u_{h,x} u_{h,xx} + \frac{\delta}{4} u_{h,xxxx} - \frac{\gamma}{12} u_{h,xxxxt} \right) = 0. \tag{32}$$

In Figure 5, we illustrate some artifacts of the numerical discretization for the pure BBM equation ($\delta = 0$). In Figure 5(a), one can observe a small dispersive tail coming mainly from nonlinear terms discretization. The amplitude of the tail is related to the order of the method. Taking Δx ten times smaller leads the reduction of the amplitude by two orders of magnitude, as it can be observed in Figure 5(b). The explanation of these phenomena is contained in the straightforward analysis of the effective Equation (32).

DOI: 10.1002/fld

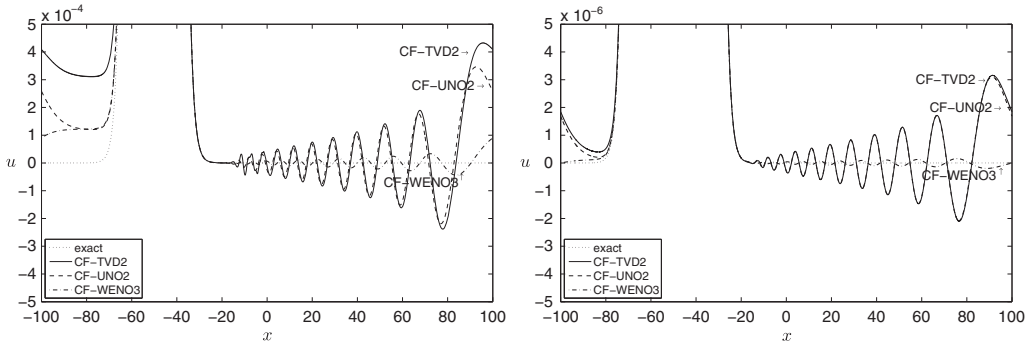

(a) $\Delta x = 0.1,\ \Delta t = 0.1$ (b) $\Delta x = 0.01,\ \Delta t = 0.01$

Figure 5. Dispersive artifacts of the equivalent equation: (a) $\Delta x = 0.1$, $\Delta t = 0.1$ and (b) $\Delta x = 0.01$, $\Delta t = 0.01$. . . . : analytical solution; —: CF-TVD2; - -:CF-UNO2; -·-:CF-WENO3.

We underline that the smallest tail is produced by the m scheme and the largest by the KT scheme. This shortcoming can be further reduced by UNO2 or WENO3 reconstruction procedures. We conclude that a detailed study of solitary wave interactions would require a combination of a higher-order method with a finer grid resolution.

4.4. Solitary wave overtaking collisions

The solitary wave solutions (also known as solitons) of the celebrated KdV equation ($\alpha = \beta = \delta = 1$ and $\gamma = 0$) have a well-known property to interact in an elastic way during an overtaking collision. In other words, the solitary waves retain their initial shape after the interaction (cf. [46]). Contrary to the KdV equation, the overtaking collision of two solitary waves of the BBM model and, in general, of the KdV–BBM equation is not elastic. Interacting solitary waves change in shape, and also a small dispersive tail appears after the process. However, a nonlinear phase shift can be still observed even in the KdV–BBM equation.

Here, we study the overtaking collision of two solitary waves of the KdV–BBM equation with $\alpha = \beta = \gamma = \delta = 1$. Solitary waves are located initially at $X_1 = -50$ and $X_2 = 50$ with speeds $c_s = 1.5$ and $c_s = 1.1$, respectively. At $t = 0$, we have two well-separated pulses, and the wave behind (left) propagates faster. Space and time variables are discretized with $\Delta x = \Delta t = 0.01$ to capture this process accurately. The solution is computed using the CF scheme and three types of reconstruction: TVD2 with van Albada limiter, UNO2 reconstruction with MinMod limiter and WENO3 method, and with the third-order explicit SSP-RK method.

The invariant $I_1^h = 18.915498698$ is conserved with the digits shown in all cases. With the invariant I_2^h, the situation is slightly different: UNO2 and WENO3 schemes preserved the value $I_2^h = 15.0633$, whereas the more dissipative TVD2 reconstruction yields $I_2^h = 15.063$.

Figure 6 shows the interaction process at several time instances in the left column and the corresponding magnification of the dispersive tail in the right column. Essentially, no difference can be observed among various numerical solutions even in the magnified region, up to the graphical resolution. Additional snapshots aiming to illustrate the interaction process are shown in Figure 7. We observe that the solitary waves propagate connected as a single pulse with a single maximum for a small time interval contrary to bidirectional models [36] and to Euler equations (cf. [47]).

Figure 8 shows the 'elastic' collision of two solitons of the KdV equation ($\alpha = \beta = \delta = 1$ and $\gamma = 0$) up to $t = 600$. In this experiment, we took $\Delta x = \Delta t = 0.01$ and 0.005 by using IMEX method (29). Contrary to the analogous collision in the case of the BBM equation, we do not observe any new dispersive tails. Further magnification of the images show small artifacts of the order $\mathcal{O}(10^{-6})$. The invariants are $I_1^h = 12.280014566440$ and $I_2^h = 9.244$ for all the computations with $\Delta x = 0.01$. When a finer grid is considered, $\Delta x = 0.005$, we do not observe any improvement in the conservation of the invariant I_1^h, whereas I_2^h was 9.2442. Analogous to the conservation

DOI: 10.1002/fld

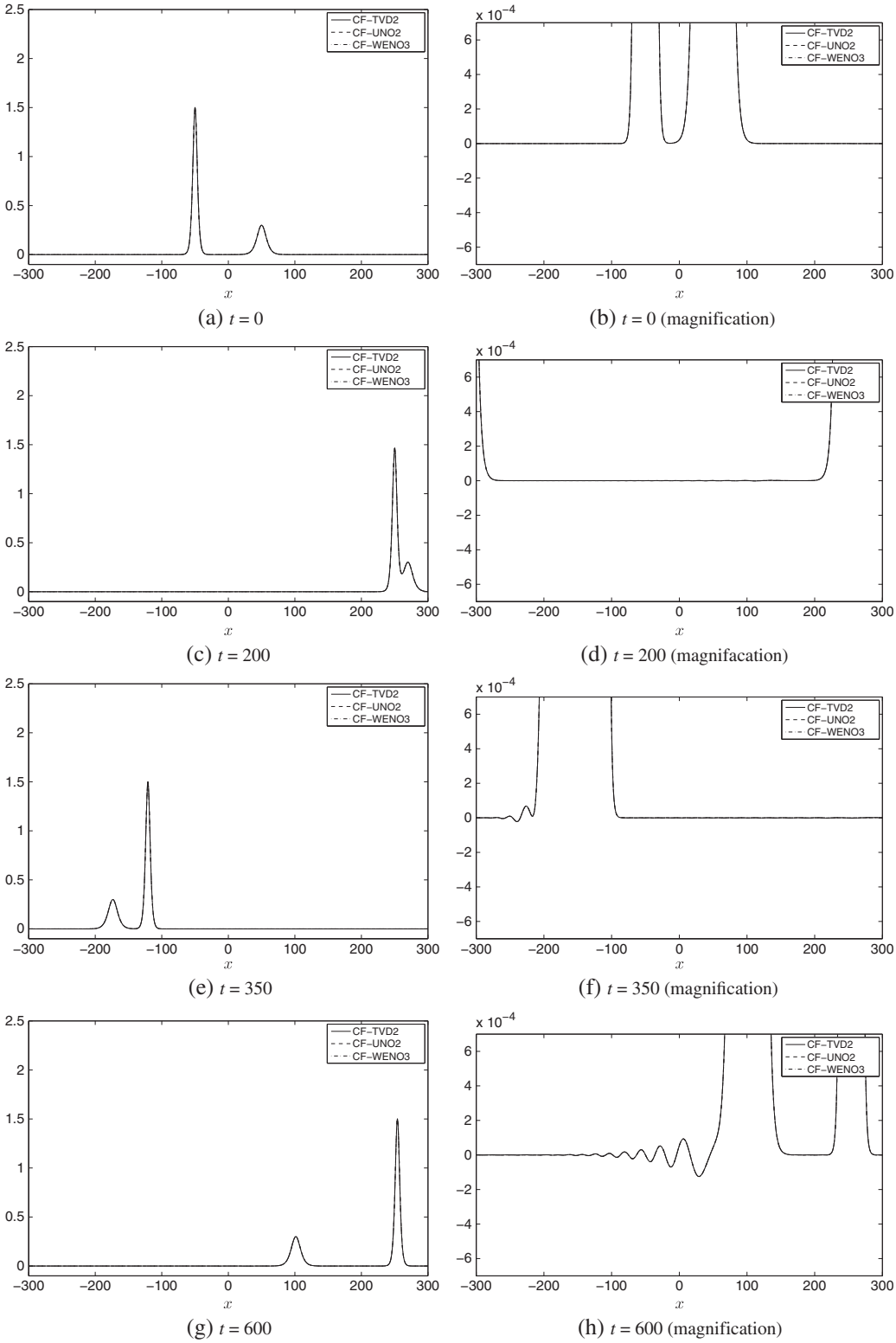

(a) $t = 0$ (b) $t = 0$ (magnification)

(c) $t = 200$ (d) $t = 200$ (magnifacation)

(e) $t = 350$ (f) $t = 350$ (magnification)

(g) $t = 600$ (h) $t = 600$ (magnification)

Figure 6. Inelastic overtaking collision of two solitary waves for the KdV–BBM equation: (a) $t = 0$, (b) $t = 0$ (magnification), (c) $t = 200$, (d) $t = 200$ (magnification), (e) $t = 350$, (f) $t = 350$ (magnification), (g) $t = 600$, and (h) $t = 600$ (magnification).

DOI: 10.1002/fld

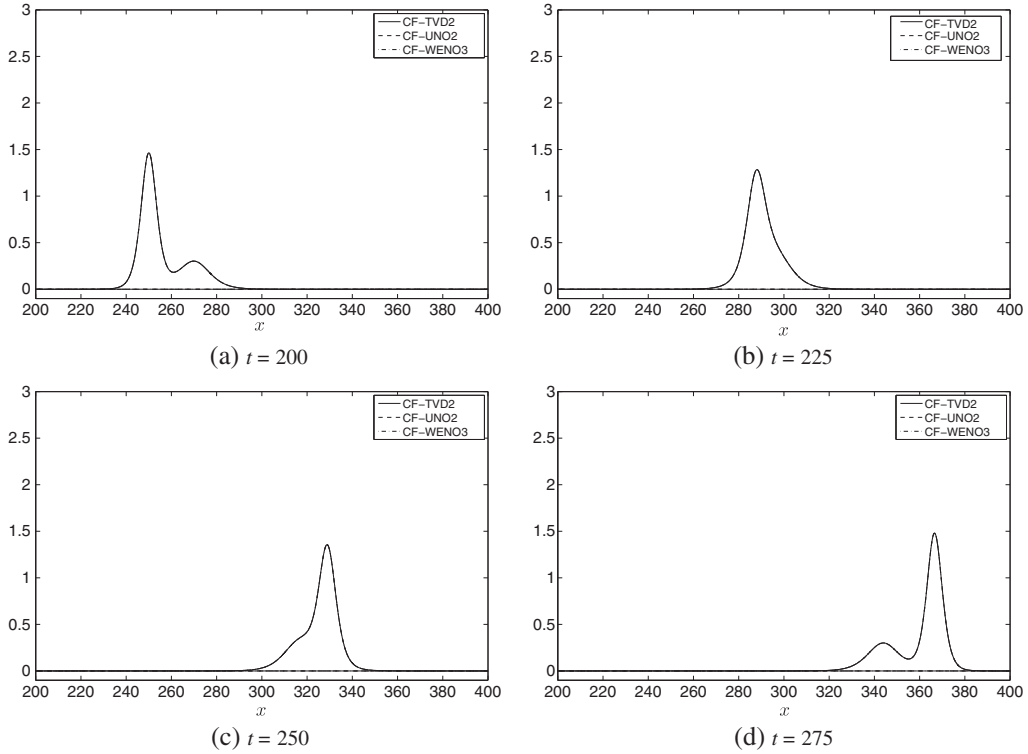

(a) $t = 200$ (b) $t = 225$

(c) $t = 250$ (d) $t = 275$

Figure 7. Inelastic overtaking collision of two solitary waves for the KdV–BBM equation (detailed view): (a) $t = 200$, (b) $t = 225$, (c) $= 250$, and $t = 275$.

properties observed when we studied the collision for the KdV–BBM equation with the IMEX method (29), we observed that $I_1^h = 18.915498698945$, but no other improvement was observed in the invariant $I_2^h = 15.0633$.

4.5. Dispersive shock formation

It was proven that smooth solutions to the KdV equation tend to become highly oscillatory as the parameter δ tends to zero (cf. [48]). These oscillatory solutions are sometimes referred to in the literature as dispersive shock waves. In this section, we study numerically this special class of solutions. Recently, a discontinuous Galerkin method was employed to study the same problem [15] in the classical setting of the KdV equation.

Namely, we consider the KdV–BBM equation with $\alpha = \beta = 1$, $\gamma = 10^{-5}$, and $\delta = 0$. A solitary wave solution (3) is taken as an initial condition with parameters $\alpha = \beta = \gamma = 1$, $\delta = 0$, and $c_s = 1.3$. We underline that this initial condition is not an exact solution to the BBM equation under consideration, because the coefficient γ is different. A fine grid with $\Delta x = 0.001$ is required to observe this phenomenon. We note that even much more accurate schemes [15] require almost the same resolution. Figure 9 shows the formation of a dispersive shock wave. The numerical solution is computed with four different methods: the m scheme and the CF scheme with TVD2, UNO2, and WENO5 reconstructions. The KT flux was also tested, producing almost identical to that of the CF scheme. In all the cases, we took $\Delta t = \Delta x/10$ except in the case of the WENO5 reconstruction where $\Delta t = \Delta x/2$.

The invariant $I_1^h = 7.493997530$ conserving the digits shown during all simulations for all numerical schemes was tested. The behavior of I_2^h is considerably different. Figure 10 (left) shows that, from the time the dispersive shock was formed, all numerical schemes, except the m scheme, lose the conservation of the invariant I_2^h. As for the m scheme, the I_2^h invariant was conserved to one decimal digit, during the whole simulation (see Figure 10(b)).

DOI: 10.1002/fld

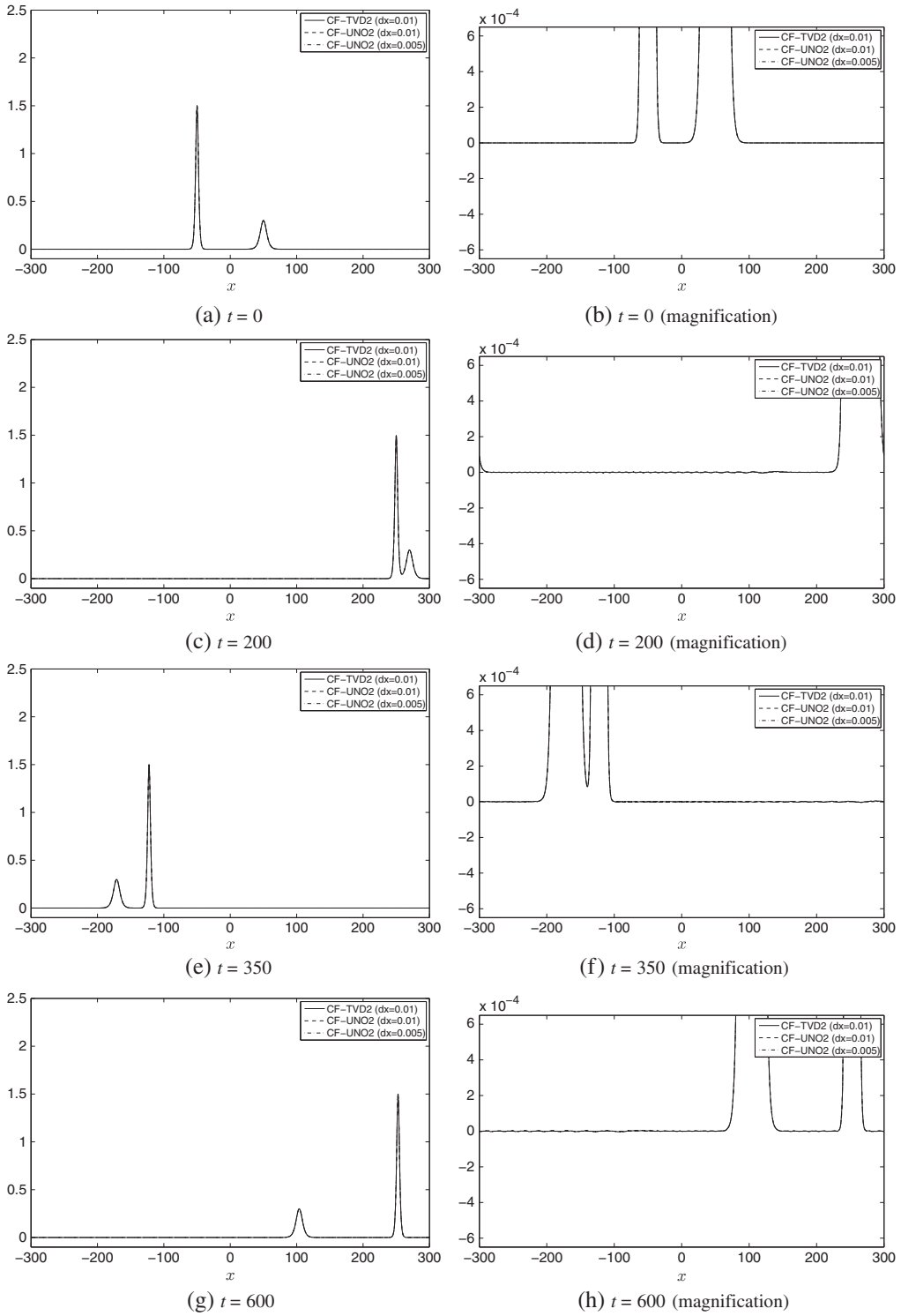

(a) $t = 0$ (b) $t = 0$ (magnification)

(c) $t = 200$ (d) $t = 200$ (magnification)

(e) $t = 350$ (f) $t = 350$ (magnification)

(g) $t = 600$ (h) $t = 600$ (magnification)

Figure 8. Elastic overtaking collision of two solitary waves computed with the KdV equation: (a) $t = 0$, (b) $t = 0$ (magnification), (c) $t = 200$, (d) $t = 200$ (magnification), (e) $t = 350$, (f) $t = 350$ (magnification), (g) $t = 600$, and (h) $t = 600$ (magnification).

DOI: 10.1002/fld

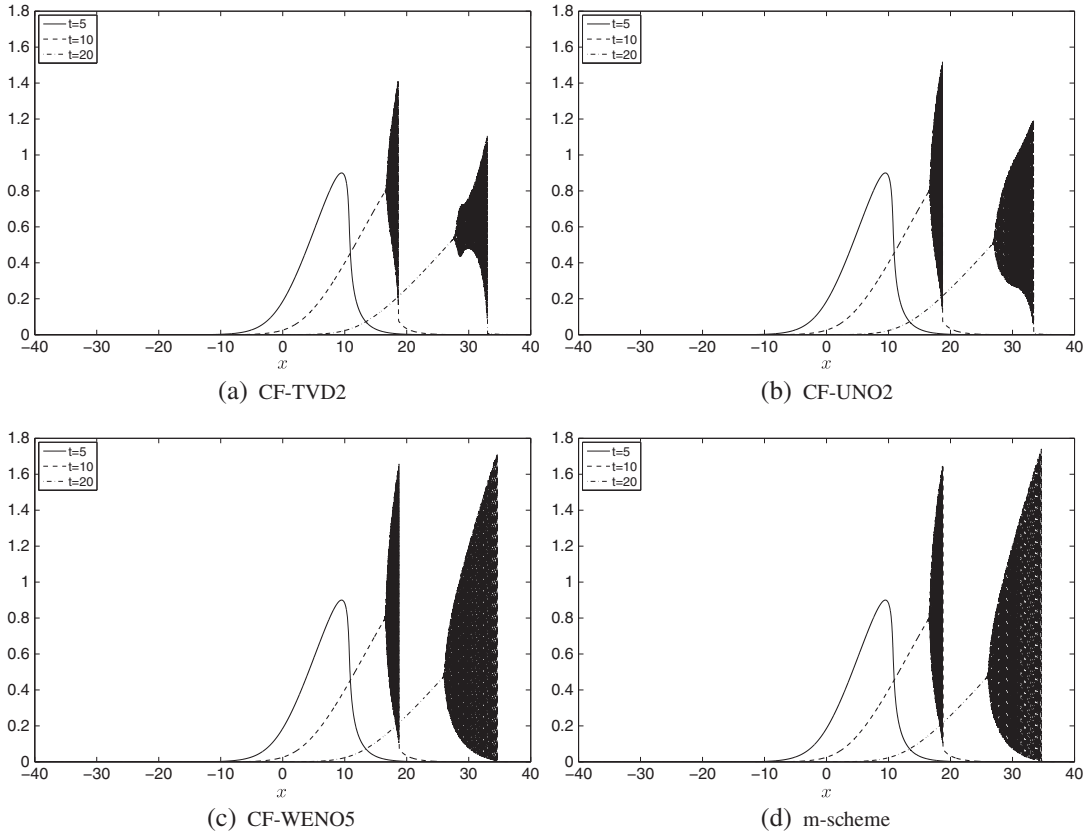

(a) CF-TVD2 (b) CF-UNO2

(c) CF-WENO5 (d) m-scheme

Figure 9. Near the zero dispersion limit, BBM equation: (a) CF-TVD2, (b) CF-UNO2, (c) CF-WENO5, and (d) m scheme.

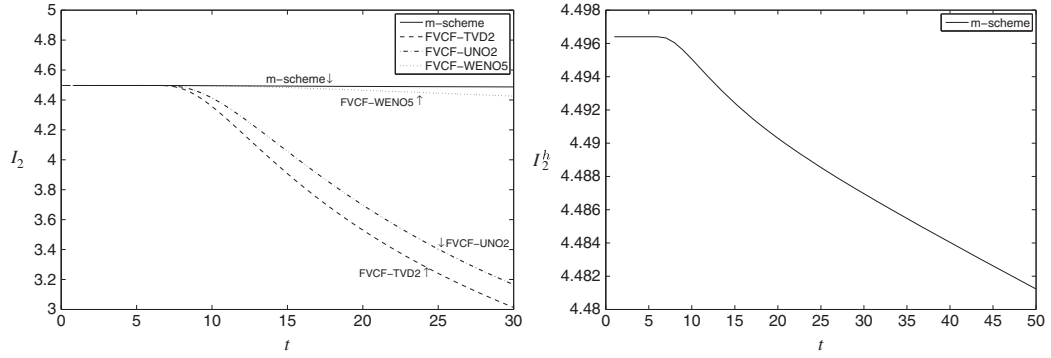

Figure 10. Evolution of I_2^h.

On the other hand, when a solitary wave solution evolves for longer time intervals, using, for example, the m scheme, we observe that solitary wave-like structures are formed (cf., Figure 11) while retaining the conservation of the invariant I_2^h up to one digit. Analogous behavior is observed for the KdV equation where general initial conditions evolved into series of solitary waves (cf. [46]).

In Figure 12, we present the same experiment for the KdV equation ($\alpha = \beta = 1$, $\gamma = 0$, and $\delta = 10^{-5}$) where the time integration is performed with the IMEX method (29) up to $T = 20$ with discretization parameters $\Delta x = 0.001$ and $\Delta t = \Delta x/2$. We observe that the invariant I_2^h is conserved with slightly less accuracy, whereas the $I_1^h = 6.572670686045$. When we use the IMEX method (29) and the m scheme in the case of the BBM equation, we observe that the invariant I_2^h

DOI: 10.1002/fld

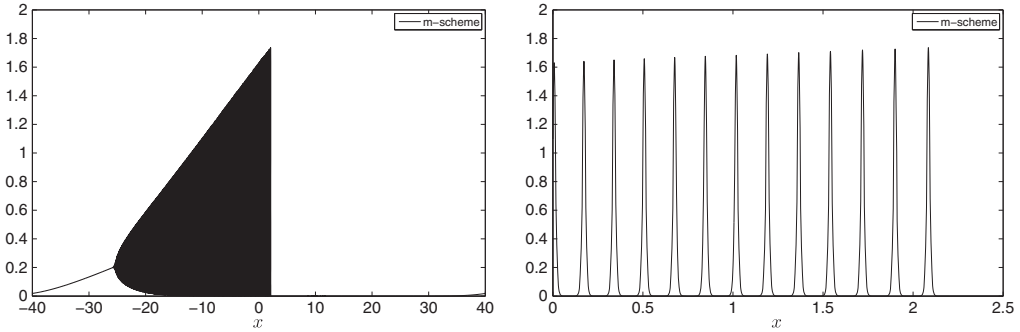

(a) m-scheme $t = 50$ (b) m-scheme $t = 50$(magnification)

Figure 11. Near the zero dispersion limit: (a) m scheme, $t = 50$ and (b) m scheme, $t = 50$ (magnification).

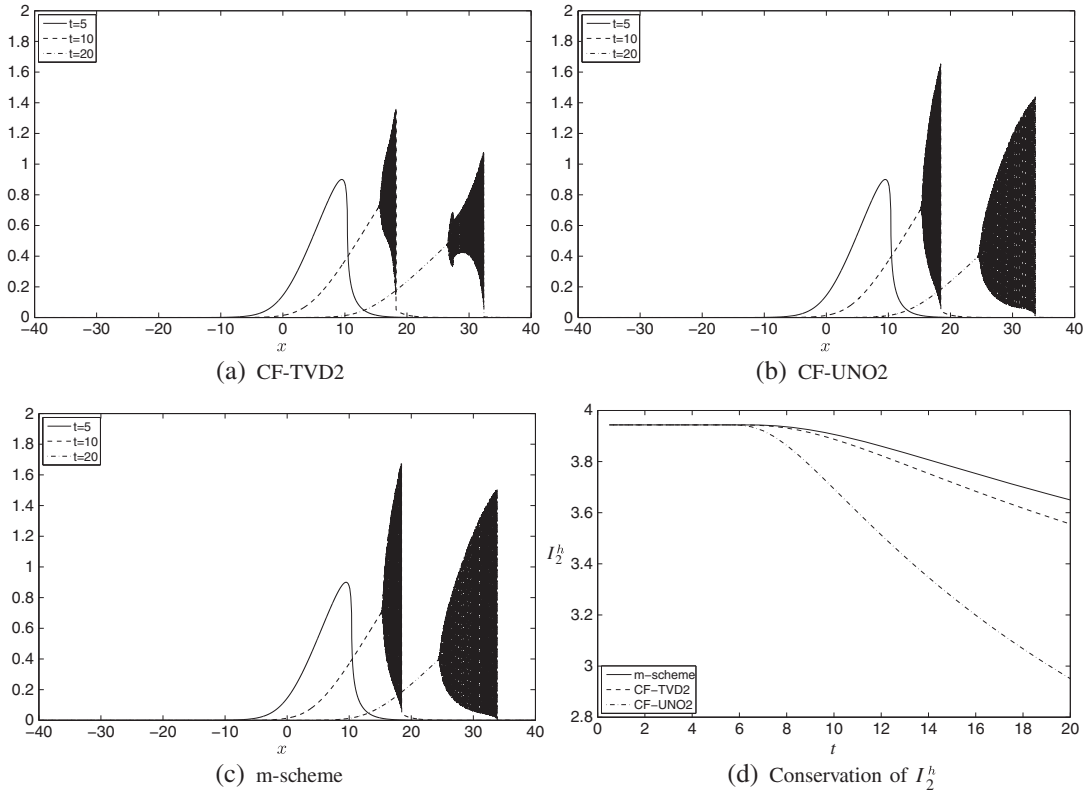

(a) CF-TVD2 (b) CF-UNO2

(c) m-scheme (d) Conservation of I_2^h

Figure 12. Near the zero dispersion limit, KdV equation: (a) CF-TVD2, (b) CF-UNO2, (c) m scheme, and (d) conservation of I_2^h.

conserves two digits, $I_2^h = 4.49$, whereas $I_1^h = 7.493997530374$ conserves the digits shown. Thus, we conclude that, in this experiment (as also observed in all previous ones), the use of the IMEX method might improve the conservation of mass.

5. CONCLUSIONS

The main scope of the present article is to extend the framework of finite volume methods to scalar unidirectional dispersive models. We chose the celebrated BBM–KdV Equation (2) as an important representative model arising in the water wave theory and having all main features of dispersive wave equations.

DOI: 10.1002/fld

The BBM–KdV equation can be also viewed as a dispersive perturbation of the inviscid Burgers equation. Consequently, our method relies on classical finite volume schemes that discretize the advection operator. Then, a special treatment was proposed for the KdV dispersion term, whereas an elliptic operator inversion per time step was required for the BBM dispersion, hence providing a physical regularization to numerical solutions. We propose and implement also several methods to obtain high-order accurate schemes.

The proposed discretization procedure is validated by comparisons with an analytical solitary wave solution. The order of convergence is measured, and invariant preservation is studied extensively. The numerical method is applied to several important test cases such as a solitary wave propagation and a dispersive shock formation. We also make use of proposed higher-order extensions to study the overtaking solitary waves collision for the KdV-BBM equation.

The extension to more realistic bidirectional wave propagation models such as Boussinesq-type equations [4, 36, 49, 50].

ACKNOWLEDGEMENTS

D. Dutykh acknowledges the support from the French Agence Nationale de la Recherche, project MathOcean (grant ANR-08-BLAN-0301-01), Ulysses Program of the French Ministry of Foreign Affairs under project 23725ZA, and CNRS PICS project no. 5607. The work of Th. Katsaounis was partially supported by the European Union FP7 Program Capacities(REGPOT 2009-1), through ACMAC (http://acmac.tem.uoc.gr).

This work was supported by the Publishing Arts Research Council (98–1846389).

REFERENCES

1. Korteweg D, de Vries G. On the change of form of long waves advancing in a rectangular canal, and on a new type of long stationary waves. *Philosophical Magazine* 1895; **39**(5):422–443.
2. Benjamin T, Bona J, Mahony J. Model equations for long waves in nonlinear dispersive systems. *Philosophical Transactions of the Royal Society of London* 1972; **272**:47–78.
3. Boussinesq J. Théorie des ondes et des remous qui se propagent le long d'un canal rectangulaire horizontal, en communiquant au liquide contenu dans ce canal des vitesses sensiblement pareilles de la surface au fond. *Journal de Mathématiques Pures et Appliquées* 1872; **17**:55–108.
4. Peregrine DH. Long waves on a beach. *Journal of Fluid Mechanics* 1967; **27**:815–827.
5. Bona J, Chen M, Saut J. Boussinesq equations and other systems for small-amplitude long waves in nonlinear dispersive media. I: derivation and linear theory. *Journal of Nonlinear Science* 2002; **12**:283–318.
6. Bona JL, Pritchard W, Scott L. Numerical schemes for a model for nonlinear dispersive waves. *Journal of Computational Physics* 1985; **60**:167–186.
7. Wei G, Kirby JT, Grilli ST, Subramanya R. A fully nonlinear Boussinesq model for surface waves. Part 1. Highly nonlinear unsteady waves. *Journal of Fluid Mechanics* 1995; **294**:71–92.
8. Bona J, Dougalis V, Mitsotakis D. Numerical solution of, KdV–KdV systems of Boussinesq equations: I. The numerical scheme and generalized solitary waves. *Mathematics and Computers in Simulation* 2007; **74**:214–228.
9. Mitsotakis D. Boussinesq systems in two space dimensions over a variable bottom for the generation and propagation of tsunami waves. *Mathematics and Computers in Simulation* 2009; **80**:860–873.
10. Avilez-Valente P, Seabra-Santos F. A high-order Petrov–Galerkin finite element method for the classical Boussinesq wave model. *International Journal for Numerical Methods in Fluids* 2009; **59**:969–1010.
11. Ozkan-Haller H, Kirby J. A Fourier–Chebyshev collocation method for the shallow water equations including shoreline runup. *Applied Ocean Research* 1997; **19**:21–34.
12. Pelloni B, Dougalis V. Numerical modelling of two-way propagation of nonlinear dispersive waves. *Mathematics and Computers in Simulation* 2001; **55**:595–606.
13. Dutykh D, Dias F. Dissipative Boussinesq equations. *Comptes Rendus Mecanique* 2007; **335**:559–583.
14. Nguyen H, Dias F. A Boussinesq system for two-way propagation of interfacial waves. *Physica D* 2008; **237**(18):2365–2389.
15. Yan J, Shu CW. A local discontinuous Galerkin method for KdV type equations. *SIAM Journal of Numerical Analysis* 2002; **40**:769–791.
16. Levy D, Shu CW, Yan J. Local discontinuous Galerkin methods for nonlinear dispersive equations. *Journal of Computational Physics* 2004; **196**(2):751–772.
17. Eskilsson C, Sherwin S. Spectral/hp discontinuous Galerkin methods for modelling 2D Boussinesq equations. *Journal of Computational Physics* 2006; **212**(2):566–589.
18. Bellotti G, Brocchini M. On the shoreline boundary conditions for Boussinesq-type models. *International Journal for Numerical Methods in Fluids* 2001; **37**(4):479–500.
19. Erduran KS, Ilic S, Kutija V. Hybrid finite-volume finite-difference scheme for the solution of Boussinesq equations. *International Journal for Numerical Methods in Fluids* 2005; **49**:1213–1232.

DOI: 10.1002/fld

20. Benkhaldoun F, Seaid M. New finite-volume relaxation methods for the third-order differential equations. *Communications on Computational Physics* 2008; **4**:820–837.
21. Tonelli M, Petti M. Hybrid finite-volume finite-difference scheme for 2DH improved Boussinesq equations. *Coastal Engineering* 2009; **56**:609–620.
22. Shiach JB, Mingham CG. A temporally second-order accurate Godunov-type scheme for solving the extended Boussinesq equations. *Coastal Engineering* 2009; **56**:32–45.
23. Brenier Y, Levy D. Dissipative behavior of some fully non-linear KdV-type of equations. *Physica D* 2000; **137**:277–294.
24. Nessyahu H, Tadmor E. Nonoscillatory central differencing for hyperbolic conservation laws. *Journal of Computational Physics* 1990; **87**(2):408–463.
25. Kurganov A, Tadmor E. New high-resolution central schemes for nonlinear conservation laws and convection–diffusion equations. *Journal of Computational Physics* 2000; **160**(1):241–282.
26. Ghidaglia JM, Kumbaro A, Coq GL. Une méthode volumes-finis à flux caractéristique pour la résolution numérique des systèmes hyperboliques des lois de conservation. *Comptes Rendus de l'Académie des Sciences - Series I - Mathematics* 1996; **322**:981–988.
27. Ghidaglia JM. Innovative methods for numerical solution of partial differential equations. In *Flux schemes for solving monlinear systems of conservation laws, in Innovative Methods for Numerical Solution of Partial Differential Equations*. WORLD SCIENTIFIC: Singapore, 2001; 232–242.
28. Sweby P. High resolution schemes using flux limiters for hyperbolic conservation laws. *SIAM Journal on Numerical Analysis* 1984; **21**(5):995–1011.
29. Harten A, Osher S. Uniformly high-order accurate nonscillatory schemes, I. *SIAM Journal on Numerical Analysis* 1987; **24**:279–309.
30. Liu XD, Osher S, Chan T. Weighted essentially non-oscillatory schemes. *Journal of Computational Physics* 1994; **115**:200–212.
31. Shu CW, Osher S. Efficient implementation of essentially non-oscillatory shock-capturing schemes. *Journal of Computational Physics* 1988; **77**:439–471.
32. Gottlieb S, Shu CW, Tadmor E. Strong stability-preserving high-order time discretization methods. *SIAM Review* 2001; **43**:89–112.
33. Ascher U, Ruuth S, Spiteri R. Implicit-explicit Runge–Kutta methods for time-dependent partial differential equations. *Applied Numerical Mathematics* 1997; **25**:151–167.
34. Fetecau R, Levy D. Approximate model equations for water waves. *Communications in Mathematical Sciences* 2005; **3**:159–170.
35. Bona J, Dougalis V. An initial- and boundary value problem for a model equation for propagation of long waves. *Journal of Mathematical Analysis and Applications* 1980; **75**:503–522.
36. Dutykh D, Katsaounis T, Mitsotakis D. Finite volume schemes for dispersive wave propagation and runup. *Journal of Computational Physics* 2011; **230**(8):3035–3061.
37. Roe PL. Approximate Riemann solvers, parameter vectors and difference schemes. *Journal of Computational Physics* 1981; **43**:357–372.
38. Harten A, Lax P, van Leer B. On upstream differencing and Godunov-type schemes for hyperbolic conservation laws. *SIAM Review* 1983; **25**:35–61.
39. Osher S. Riemann solvers, the entropy condition, and difference approximations. *SIAM Journal on Numerical Analysis* 1984; **21**(2):217–235.
40. Ghidaglia JM, Kumbaro A, Coq GL. On the numerical solution to two fluid models via cell centered finite volume method. *European Journal of Mechanics - B/Fluids* 2001; **20**:841–867.
41. Benkhaldoun F, Quivy L. A non homogeneous Riemann solver for shallow water and two phase flows. *Flow, Turbulence and Combustion* 2006; **76**:391–402.
42. Kolgan N. Application of the minimum-derivative principle in the construction of finite-difference schemes for numerical analysis of discontinuous solutions in gas dynamics. *Uchenye Zapiski TsaGI [Scientific Notes of Central Institute of Aerodynamics]* 1972; **3**(6):68–77.
43. van Leer B. Towards the ultimate conservative difference scheme v: a second-order sequel to Godunov's method. *Journal of Computational Physics* 1979; **32**:101–136.
44. Shu CW. Essentially non-oscillatory and weighted essentially non-oscillatory schemes for hyperbolic conservation laws. *Advanced Numerical Approximation of Nonlinear Hyperbolic Equations* 1997:325–432. Springer Berlin / Heidelberg.
45. Spiteri RJ, Ruuth SJ. A new class of optimal high-order strong-stability-preserving time discretization methods. *SIAM Journal on Numerical Analysis* 2002; **40**:469–491.
46. Drazin PG, Johnson R. *Solitons: An Introduction*. Univ. Pr (1989): Cambridge, UK, 1989.
47. Craig W, Guyenne P, Hammack J, Henderson D, Sulem C. Solitary water wave interactions. *Physics of Fluids* 2006; **18**:57–106.
48. Venakides S. The zero dispersion limit of the Korteweg–de Vries equation with periodic initial data. *AMS Transactions* 1987; **301**:189–226.
49. Nwogu O. Alternative form of Boussinesq equations for nearshore wave propagation. *Journal of Waterway, Port, Coastal and Ocean Engineering* 1993; **119**:618–638.
50. Madsen PA, Bingham HB, Schaffer HA. Boussinesq-type formulations for fully nonlinear and extremely dispersive water waves: derivation and analysis. *Proceeding of the Royal Society of London A* 2003; **459**:1075–1104.

DOI: 10.1002/fld